Evaluating the Effect of Ionomer Chemical Composition in Silver-Ionomer Catalyst Inks toward the Oxygen Evolution Reaction by Half-Cell Measurements and Water Electrolysis

Nora C. Buggy[a], Ivy Wu[a], Yifeng Du[b], Ria Ghosh[b], Mei-Chen Kuo[a], Morgan S. Ezell[a], James M. Crawford[a], Soenke Seifert[c], Moises A. Carreon[a], E. Bryan Coughlin[b], Andrew M. Herring[a]*

*aherring@mines.edu

[a] Department of Chemical and Biological Engineering, Colorado School of Mines, 1500 Illinois Street, Golden, Colorado, 80401, United States.

[b] Department of Polymer Science and Engineering, University of Massachusetts Amherst, 120 Governors Drive, Amherst, Massachusetts, 01003, United States.

[c] X-ray Science Division, Argonne National Laboratory, 9700 S Cass Avenue, Lemont, Illinois, 60439, United States.

Abstract

The effect of anion exchange ionomer (AEI) chemistry on the kinetics of the oxygen evolution reaction (OER) was systematically studied in both half-cell and single-cell electrolysis experiments. OER was studied in 1 M K_2CO_3 at 50 °C using an array of ionomer-silver catalyst inks deposited on Ni foam. Different ionomer modifications were investigated to optimize the OER performance. The AEI used in this work features a block copolymer backbone of polychloromethylstyrene-*b*-polycyclooctene-*b*-polychloromethylstyrene which was functionalized with either benzyltrimethylammonium (TMA) or benzylmethylpiperidinium (MPRD) quaternary ammonium cations. Using an MPRD quaternary ammonium cation shifted

the rate determining step at high overpotentials, ultimately providing enhanced performance. Increasing the catalyst ink dilution was also found to substantially improve mass activity and catalyst utilization (increase from 35 to 88 A g^{-1} Ag), likely by reducing the ionomer thickness and decreasing transport resistances. In the final ionomer modification, the Ni foam substrate was leveraged to partially hydrogenate the polycyclooctene midblock to be polyethylene-like at the Ni interface. A significant increase in the electrochemical surface area (C_{dl} increased from 8.8 to 20.8 mF cm^{-2}) and performance (by 47 mA cm^{-2} or 29 A g^{-1} Ag) was observed with the incorporation of polyethylene. Kinetic results from half-cell experiments were validated via single-cell anion exchange membrane electrolysis experiments, where the optimized electrode displayed enhanced performance in both 1 M K_2CO_3 and in DI H_2O.

Keywords: oxygen evolution reaction, anion exchange ionomer, block copolymer, alkaline water electrolysis, quaternary ammonium cation

1. Introduction

Electrochemical production of hydrogen via water electrolysis is a key technology necessary for the development of a sustainable hydrogen-based energy infrastructure (1, 2). Alkaline electrolyzers, which utilize 30 – 40 wt% aqueous KOH solutions, are a commercially mature technology, but various drawbacks inherent to their architecture, such as limited lifetime, poor efficiency, large footprint, and low power density have left substantial room for improvement even for large scale hydrogen production. Proton exchange membrane (PEM) and anion exchange membrane (AEM) water electrolyzers provide enhanced conversion efficiencies with a smaller footprint. Despite the promising performance of PEM water electrolyzers (PEMWEs), the high cost of the required platinum group metal (PGM) catalysts (iridium oxide and platinum)

in addition to their corrosion-resistant cell components position PEMWEs to be prohibitively expensive for large scale commercialization (3).

[Insert Figure 1]

Anion exchange membrane water electrolyzers (AEMWEs) operate in alkaline media which allows for the utilization of less expensive, more abundant non-PGM catalysts, thus combining the advantages of alkaline electrolyzers and PEMWEs. Anion exchange membranes (AEMs) are polymer electrolytes with covalently bound cationic functional groups that facilitate the transport of anions (typically OH^- or CO_3^{2-}) across the device from cathode to anode. The electrochemical reactions in an AEMWE are the oxygen evolution reaction (OER) at the anode and the hydrogen evolution reaction (HER) at the cathode. A schematic of an AEMWE is given in Figure 1.

The half-cell reactions and overall reaction for water electrolysis in alkaline media are,

Anode reaction (OER): $4OH^- \rightarrow O_2 + 2H_2O + 4e^-$ (1)

Cathode reaction (HER): $4H_2O + 4e^- \rightarrow 2H_2 + 4OH^-$ (2)

Overall reaction: $2H_2O \rightarrow 2H_2 + O_2$ (3)

At the cathode, water is reduced to hydrogen and hydroxide ions which move across the AEM to the anode where they are oxidized and yield oxygen, water, and electrons. Since water is both a product and reactant, water produced at the anode would ideally diffuse through the AEM to the cathode; however, electro-osmotic drag tends to carry water in the opposite direction, i.e. the direction of hydroxide ion transport, depending on the membrane thickness. Ideally, an AEMWE would utilize pure water, but in practice, the current densities achieved in pure water are poor. For this reason, AEMWEs commonly report utilizing a supporting electrolyte such as aqueous

KOH or K_2CO_3, typically 0.01 M – 1.0 M (4-6), which improves the performance compared to using water alone (7). Previous studies have shown how the kinetics for OER improve (e.g. Tafel slope decreases from *ca.* 160-274 mV dec^{-1} to 53-72 mV dec^{-1} (8)) as the pH increases from 7 (neutral water) to 14 (1 M KOH) (9, 10). Additionally, while KOH-fed electrolyzers outperform K_2CO_3-fed electrolyzers at the same molar concentration, the performance of K_2CO_3 outperforms KOH at the same pH (11). A recent modeling study suggested that the addition of OH^- reduces ohmic resistances of the AEM and catalyst layer and improves reaction kinetics by increasing the electrochemically active surface area (12).

In the case of using a supporting electrolyte such as K_2CO_3, after hydroxide ions are produced at the cathode, a mixture of hydroxide, along with the present carbonate (and possibly bicarbonate) ions diffuse toward the anode. At the anode, carbonate and bicarbonate anions are purged from the system via the following reactions (13, 14):

$$CO_3^{2-} + H_2O \rightleftharpoons HCO_3^- + OH^- \quad (4)$$

$$HCO_3^- \rightleftharpoons CO_2 + OH^- \quad (5)$$

Hydroxide ions are then oxidized to water and O_2 according to reaction (1). The self-purging reactions are well documented for anion exchange membrane fuel cells (AEMFCs) (15). In the case of the oxygen reduction reaction (ORR) in AEMFCs, and likely in OER in AEMWEs, it is assumed that HCO_3^- and CO_3^{2-} are not directly participating in the electrochemical reactions (16, 17). The reactions for electrolysis with carbonate-based electrolytes where CO_3^{2-} ions participate directly to realize the production of both H_2, O_2 and CO_2 are extremely sluggish and require a cell voltage upwards of 3 V (10, 18). Operating beneath this voltage further ensures that during

electrolysis with supporting carbonate-based electrolytes, only OH^- participates via the conversion of CO_3^{2-} and HCO_3^- in equations (4) and (5).

Much recent work has focused on the development of AEMs with high ionic conductivity, water management, mechanical integrity, and resiliency to hydroxide-induced degradation mechanisms. Fewer reports exist on the optimization of the ionomer in the catalyst layer of the electrode. Previous studies have shown the ionomer can influence reaction kinetics by affecting several transport and interfacial phenomena. The ionomer in the catalyst layer will affect the transport of OH^- ions, water, and oxygen to and from the catalyst surface. It is known that the ionomer also influences the effective utilization of the catalyst surface and the double-layer capacitance, which ultimately influence the electrochemical reaction kinetics (19). Specifically, Nafion® has been shown to adsorb to Pt surfaces and reduce the available catalyst active area (20). Additionally, the ionomer can influence reaction kinetics by the interface it forms with the catalyst surface. The environment surrounding the catalytic sites, i.e. the secondary coordination sphere, can substantially impact the catalyst performance (21). Ionomer within the secondary coordination sphere can facilitate non-covalent interactions to stabilize intermediates and improve catalytic activity (22). Recent work has shown the ionomer structure, specifically the steric bulk of the ionic moiety, can intrinsically modulate reaction kinetics and influence both activity and selectivity for CO_2 reduction and HER (23). Fundamental studies have been conducted using density functional theory (DFT) (24) and/or using experimental techniques such as rotating disk electrodes (RDEs) (25, 26), where it has been shown ionomer adsorption to the catalyst surface can play a significant role in performance and available catalyst active area. Recently, a study using quaternary ammonium cations (QACs) with long tethered groups (triethylammonium) demonstrated that they were worse than shorter groups

(trimethylammonium) because when adsorbed to the catalyst the longer ethyl group blocked more active sites (24). The authors suggested utilizing other bulkier QACs that may be more sterically hindered from adsorption would be beneficial. In contrast, a recent microelectrode and AEMFC study showed triethylammonium outperformed trimethylammonium by reducing cation adsorption (27). While insight from different approaches is useful and can correlate to real device performance under the right conditions (28), it is also known that the catalyst and ionomer kinetics and performance in an RDE study can diverge significantly from the activity in an operating device (29). Therefore, many optimization studies are done in an operating cell (30). Recently, Huang et al. optimized the water uptake of the ionomer incorporated in both the anode (31) and cathode (32) in an AEMWE by balancing a high ion exchange capacity (IEC) with crosslinking to reduce swelling. Faid et al. used an in-situ half-cell approach by adding a reference electrode to an AEMWE experiment to separately optimize ionomer loading for OER and HER (33).

There are many disadvantages to optimizing a single electrode using full cell tests. It can be challenging to separate the performance of the anode from the cathode. It is a more time intensive process to optimize one electrode at a time. Furthermore, MEA preparation and cell assembly introduce additional variables to the system. A more efficient solution is to perform ex-situ half-cell studies, where the electrochemical performance of each electrode can be isolated. These experiments also reduce the number of interfaces and therefore contributions to the electrochemical performance. Studies of this nature have been performed more frequently for ORR in acidic media (34-36) and more recently for ORR (37) and OER (38) in alkaline media and HER in acidic media (39).

This study reports for the first time the optimization of ionomer structures using a separated anode half-cell approach. We utilize a tunable triblock copolymer system of polychloromethylstyrene-*b*-polycyclooctene-*b*-polychloromethylstyrene (PCMS-*b*-PCOE-*b*-PCMS) (40) that we previously modified via hydrogenation (41) to fabricate a polyethylene (PE) triblock copolymer-based anion exchange membrane which excellent mechanical properties in water for AEMWE applications. It is advantageous to utilize an ionomer with similar chemical composition in the catalyst layer (CL) to reduce interfacial resistances in a membrane electrode assembly. Therefore, this work utilizes the same PCOE-based triblock copolymer precursor, which is post functionalized with quaternary ammonium cations (QACs) and incorporated as the anion exchange ionomer.

Electrodes for AEMWEs are made by coating a porous support in a catalyst-ionomer ink. Commonly implemented porous substrates include carbon paper or cloth for the cathode, or metal felts, foams, or meshes of stainless steel, titanium, or nickel for the anode (6). Using an electrically conductive porous support is essential because the widely porous interconnected framework allows for gas and fluid transport while simultaneously providing electrical conductivity (42). In addition to possessing high surface area and electrical conductivity, porous Ni foams are an attractive substrate because of their resistance to corrosion at high pH (43-46) and excellent OER performance (47-50). Therefore, this work utilizes a Ni foam electrode coated in a catalyst-ionomer ink.

Our previous work has highlighted interactions that can occur between ionomers and Ag nanoparticles (51) and the implications of those interactions on the thin film morphology on Ag surfaces (52). In this work, the electrochemical performance toward OER of various Ag-ionomer catalyst inks on Ni foam are evaluated in half-cell experiments. The ionomer is optimized

through a series of modifications including different backbone chemistries and QAC functionalities. The two QACs compared in this work are benzyltrimethylammonium (TMA) and benzylmethylpiperidinium (MPRD). The effect of ink dilution, which relates to the thickness of the ionomer thin film coating the Ag catalyst particles, was also investigated. Improvements in kinetics and performance are discussed, and the final optimized electrode was incorporated into an AEMWE. The results are summarized, and recommendations are provided for tuning ionomer-Ag interactions to develop a favorable interface and enhanced electrochemical performance.

2. Experimental Methods

2.1 Materials

Ni foam substrates (thickness = 0.3mm) were purchased from MSE Supply Company. The substrates were pre-cleaned by sonicating for 30 min in acetone followed by sonicating for 30 min in 2M HCl and then rinsing in DI water. Ag nanopowder (average particle size 20 – 40 nm) was purchased from Alfa Aesar and used as received. The following reagents were purchased from various vendors and used as received. *N*-methylpiperidine ($C_6H_{13}N$, 99%), trimethylamine solution (C_6H_3N, 50wt% in water), chloroform ($CHCl_3$, >99%), methanol, (MeOH, CH_3OH, ACS grade), and 1,1,2,2-tetrachloroethane (reagent grade ≥98.0%). The block copolymers used in this work, including polychloromethylstyrene-*b*-polycyclooctene-*b*-polychloromethylstyrene (PCMS-*b*-PCOE-*b*-PCMS) and polyisoprene-*ran*-polychloromethylstyrene (PIp-*ran*-PCMS), were synthesized via methods published previously (53, 54), which are re-described briefly in the supporting information. Gel permeation chromatography (GPC), ^{1}H NMR, the chemical composition, and IEC of both ionomers can be viewed in Figures S1-S4 and Tables S1-S2. The

base triblock copolymer used for the AEM fabrication, Tuffbrane™, was supplied by Spark Ionx Inc.

2.2 Environmental scanning electron microscopy (ESEM) and energy dispersive spectroscopy (EDS)

Scanning electron microscopy images were collected using an FEI Quanta 600 operating under low vacuum at 25 kV. EDS was performed with an element EDAx energy dispersive spectroscope. Standard parameters were used to quantify elements using EDAx Genesis software.

2.3 Brunauer−Emmet−Teller (BET) Surface Area

The BET surface area of Ni foam was extracted from N_2 isotherms. An ASAP 2020 porosimeter (Micromeritics, Norcross, GA, USA) was used to collect nitrogen isotherms at 77 K. Prior to analysis, the sample was degassed for 8 h at 150 °C under high vacuum. Surface areas were calculated using the BET method following criterion described previously (55).

2.4 Half-Cell Electrode Fabrication

Ni foam substrates were cut to a size of 3.0 cm x 4.5 cm (13.5 cm^2). This is the size necessary to contact the working electrodes in the FlexCell® apparatus, described in section **3.2**.

For Ag-ionomer catalyst ink coated electrodes, Ag nanopowder (Alfa Aesar, average particle size 20 - 40 nm) was added to a 10 mg mL^{-1} solution of PCMS-*b*-PCOE-*b*-PCMS in $CHCl_3$ and sonicated for 1 h prior to dip coating. The ionomer:catalyst (I:C) ratio of 15:85 was kept constant in all experiments, and the target loading of Ag was either 2.5 or 1.5 mg cm^{-2}. In all dip-coating processes, between each dip the electrodes were placed on a hot plate at 60 °C to evaporate the

$CHCl_3$ solvent. After the total amount of polymer-Ag ink was deposited on each electrode, they were dried under vacuum for 12 h to remove any residual solvent.

To partially hydrogenate the PCOE midblock to PE, electrodes with PCMS-*b*-PCOE-*b*-PCMS-Ag ink were hydrogenated by utilizing the Ni foam substrate as the hydrogenation catalyst. Electrodes were placed in a vessel purged for 30 min with $N_{2(g)}$, followed by purging with $H_{2(g)}$ for 30 min. The vessel was then sealed with a balloon which was inflated with $H_{2(g)}$, and the samples reacted under $H_{2(g)}$ for 24 h.

The Ag-polymer coated electrodes were quaternized in 50 wt% trimethylamine/water to yield benzyltrimethylammonium cationic moieties, or in 50 vol% *N*-methylpiperidine/MeOH to yield benzylmethylpiperidinium cationic moieties. Electrodes were submerged in solution for 48 h at room temperature, then thoroughly rinsed in DI water and dried under vacuum for 12 h.

2.5 Half-Cell Experiments

Half-cell tests were performed using a PTFE FlexCell® (Gaskatel, gmBH). 3.0 x 4.5 cm electrodes were placed in the cell. A 3 cm^2 active area was isolated by the silicone gaskets. The current densities in this study are normalized to this planar surface area.

The working electrode (WE), counter electrode (CE), and reference electrode (RE) were the Ni foam electrodes, a Pt wire, and a Pt-H_2 HydroFlex® reference electrode (Gaskatel, gmBH) respectively. Prior to experiments, the working electrodes were soaked in 1 M K_2CO_3 for 1 h to exchange from the Cl^- form to the CO_3^{2-} form. Once the cell was assembled with the WE, 1 M K_2CO_3 electrolyte was added to the cell and heated to 50 °C and allowed to equilibrate at that temperature for 1 h prior to beginning experiments. A stir bar was added to the electrolyte compartment to reduce noise from gas bubble formation during OER. A VMP-300 potentiostat

(Biologic) was used for electrochemical measurements. Linear sweep voltammetry (LSV) was collected at 5 mV s^{-1}. The reaction kinetics can be described by the Butler-Volmer equation (58):

$$j = j_{fwd} - j_{rev} = j_0 exp\left(\frac{\alpha\eta F}{RT}\right) - j_0 exp\left(\frac{-(1-\alpha)\eta F}{RT}\right) \quad (6)$$

Where j_0 is the exchange current density, α is the charge transfer coefficient, η is the overpotential, R is the ideal gas constant, and T is the temperature. At large overpotentials ($\eta >$ 15 mV) where the reactions become irreversible, the Butler-Volmer equation simplifies to the Tafel equation, expressed in common logarithmic terms as:

$$\eta = \left(\frac{2.303RT}{\alpha F}\right) logj - \left(\frac{2.303RT}{\alpha F}\right) logj_0 \quad (7)$$

Tafel equation fits were calculated for both 100% iR compensated LSVs (shown in the main text) and iR-uncompensated LSVs (available in the supporting information). Electrochemical impedance spectroscopy (EIS) was performed at open circuit voltage (OCV) to determine the solution resistance used for performing iR correction.

Cyclic voltammetry (CV) collected at 10, 20, 30, and 50 mV s^{-1} in the potential range of 1.12-1.22 V was used to calculate the double layer capacitance (C_{dl}) as an estimate of electrochemical surface area. C_{dl} was calculated by plotting $j_A - j_C$, or Δj, at 1.17 V versus the scan rate, where the linear slope = $2C_{dl}$.

2.6 Anion Exchange Membrane Fabrication

The AEMs used in this work were fabricated from a block copolymer precursor, Tuffbrane™, supplied by Spark Ionx. Membranes were produced by suspending the polymer in 1,1,2,2-tetrachloroethane (TeCA). Films were solution cast onto Teflon® coated PEEK sheets with a dropper pipette and were partially covered by a glass plate and allowed to dry and ambient

conditions. Once dry, another Teflon® sheet was placed on top of the polymer film on the Teflon® coated PEEK sheet and was then hot pressed at 160 °C and 90 psi for 5 minutes, four times. Films were then easily peeled from the sheet with an approximate thickness of 38 ± 5 um. The films were post-quaternized in 50% *N*-methylpiperidine in MeOH for 3 days at 50 °C to yield AEMs. The AEMs were washed with DI H_2O until the H_2O had a neutral pH. The membranes were then annealed in DI H_2O at 80 °C in the oven for 24 h. AEMs were stored in DI H_2O at room temperature before use.

2.7 Membrane Electrode Assembly (MEA) Fabrication

Anodes and cathodes were fabricated using the catalyst-coated substrate method. Ni foam or Toray carbon paper (TGP-H-60) was cut to a size of 5 cm^2 for use as the porous transport layer (PTL) for the anode or cathode, respectively. For the anode, Ag-ionomer catalyst inks were prepared and deposited via the same dip-coat method described above in section **2.4**. The same I:C ratio of 15:85 was used with a target Ag loading of 4 mg cm^{-2}.

For the cathode catalyst ink, platinum supported carbon (Pt/C, Tanaka TEC10E50E, 46.3% Pt) and DI water was added to a 5 mg mL^{-1} solution of polyisoprene-*ran*-polychloromethylstyrene functionalized with methylpiperidinium cations (PIp-*ran*-PCMS[MPRD]) ionomer (54, 59) in MeOH and sonicated for 1 h prior to deposition. An I:C ratio of 15:85 was used, and the target loading of Pt/C was 1.5 mg cm^{-1}. Carbon paper PTLs were placed on a hot plate at 60 °C and the catalyst ink was applied by a manual painting method. After the total amount of catalyst ink was deposited on each electrode, they were dried under vacuum for 12 h to remove any residual solvent.

The membrane electrode assemblies (MEAs) were made using a 5 cm^2 anode and cathode and an 8-9 cm^2 AEM. Before cell assembly, the Ni foam anodes were pressed at 90 psi for 1 min. The anode, cathode and membrane were then individually ion-exchanged to the CO_3^{2-} form by soaking in 1 M K_2CO_3 for 60 min.

The AEM was placed between the anode and cathode in 5 cm^2 Fuel Cell Technologies hardware between two graphite serpentine flow-fields with PTFE-coated fiberglass fabric gaskets (McMaster-Carr) with thicknesses of 152 and 380 μm for the cathode and anode side, respectively. The cell was assembled with a torque of 2.5 ft-lbs.

2.8 Single-Cell Electrolyzer Testing

MEAs were tested using a custom-built electrolysis test station. Aqueous 1 M K_2CO_3 (or MilliQ DI H_2O) was fed to both the anode and cathode at 15 mL min^{-1}. The cell and liquid feed line were heated to 50 °C and the cell was allowed to equilibrate for 1 h prior to testing. To collect polarization curves, chronopotentiometry was performed at each current step for 1 min to allow for equilibration. EIS was also performed from 10 kHz to 50 mHz at OCV to determine the high frequency resistance (HFR) to calculate the area specific resistance (ASR) of the cell.

3. Results and Discussion

3.1 Electrode Fabrication and Characterization

Most reports on AEMWEs that use porous supports normalized the current density by the planar surface area of the support (60). While this is relevant, the electrochemically active surface area of porous catalyst materials, including Ni foams, is always much larger than its geometric surface area. To characterize this, an N_2 isotherm (Figure S5) was used to calculate the BET surface area of the pristine Ni foam substrates. The BET surface area of the pristine Ni foam was

0.104 ± 0.004 m^2 g^{-1}, making the real Ni surface area *ca.* 32 times larger than the planar surface area of the substrate.

Figure 2 shows the Ni foam electrode before and after depositing Ag-ionomer catalyst ink. The SEM images highlight the large porous framework of the Ni foam substrate. After Ag-ionomer catalyst ink deposition, the Ni framework is coated in both ionomer and Ag nanoparticles. Some of the holes in the Ni foam framework are covered by a layer of Ag-ionomer ink, evident in Figure 2D.

[Insert Figure 2]

EDS was used to characterize the electrode before and after depositing an ionomer-Ag ink. The results are summarized in Table 1. The pre-cleaned Ni foam electrodes show a small percentage of oxygen, indicating partial oxidation of the Ni foam surface. After depositing Ag-ionomer ink, Ag, C, and N are detected as well.

Table 1. Surface elemental composition for Ni foam and Ag-ionomer coated Ni foam, from EDS.

Element (%)	Ni Foam	Ag-Ionomer Coated Ni Foam
Ni	97.3	54.3
O	2.7	2.6
C/N	0	17.0
Ag	0	26.1

3.2 Electrochemical Characterization: Half-Cell Experiments

The electrochemical performance of the Ni foam-coated electrodes was studied in a FlexCell® three electrode half-cell apparatus (see Figure 3). Ni foam catalyst ink-coated electrodes were used as the working electrode and a Pt wire and HydroFlex® electrode were used as the counter and reference electrodes, respectively. Aqueous 1 M K_2CO_3 was used as the electrolyte.

The catalyst inks used in this work are summarized in Table 2. The I:C ratio was kept constant at 15:85 for all the electrodes in this study. The current densities in the following experiments are normalized by the planar active surface area of the electrode, 3 cm^2, for comparison to other studies. Overpotentials are defined with respect to the OCV of the assembled half-cell, which was 1.45 V after equilibrating in 1 M K_2CO_3 at 50 °C. In the potential window studied (1.45 V – 1.85 V vs RHE), based on the electrolyte pH (~11.6), the Pourbaix diagram of Ag indicates the Ag nanoparticles will have an oxidized surface of Ag_2O_3 (56). Additionally, under these conditions Ni is oxidized to $Ni(OH)_2$ and further oxidation to NiOOH should occur beyond 1.85 V vs RHE (57). Therefore, oxidation currents from Ni and Ag do not affect the estimation of OER parameters within this potential window.

[Insert Figure 3]

Table 2. Summary of Ag-ionomer inks used in this work

Catalyst Ink[a]	Ink Dilution / mass solid:liquid	Ionomer midblock	Quaternary Ammonium Cation	Ag loading/mg cm^{-2}
PC-TM-25	1:25	PCOE	TMA	2.6 ± 0.1
PC-MP-25	1:25	PCOE	MPRD	2.6 ± 0.1
PC-TM-100	1:100	PCOE	TMA	1.6 ± 0.2
PC-MP-100	1:100	PCOE	MPRD	1.6 ± 0.2
PE-TM-100	1:100	PE[b]	TMA	1.6 ± 0.2
PE-MP-100	1:100	PE[b]	MPRD	1.6 ± 0.2

[a] PC: polycyclooctene midblock, PE: partially polyethylene midblock, TMA: trimethylammonium quaternary ammonium cation, MPRD: methylpiperidinium quaternary ammonium cation

[b] Partially hydrogenated PCOE, PE at the interface

3.2.1 Comparison of Quaternary Ammonium Cation

The first step toward optimizing the ionomer chemistry was comparing the performance of two QACs, trimethylammonium (TMA) and methylpiperidinium (MPRD). An Ag catalyst ink was made with the block copolymer precursor PCMS-*b*-PCOE-*b*-PCMS (see section **2.4** for detailed procedure) and coated onto the Ni foam substrate. The coated substrate was functionalized by quaternizing in either trimethylamine or methylpiperidine to obtain TMA or MPRD moieties. Figure 4 shows the OER linear sweep voltammograms (LSVs) of PC-TM-25 and PC-MP-25. EIS was used to determine the solution resistance for iR correction, C_{dl} and Tafel plots for Ni foam, CV scans used to calculate C_{dl}, and LSVs without iR correction can be viewed in the supporting information in Figures S6-S11. Relevant electrokinetic parameters extracted from

modeling the LSVs with the Butler-Volmer equation are summarized in Table 3 (LSVs without iR correction, in Table S3). The Tafel slope, charge transfer coefficient (α), and exchange current density (j_0) are dependent on both the potential and surface coverage of species (61). Our results indicate the presence of two distinct kinetic regimes at lower (*ca.* 0.1 – 0.2 V) and higher (*ca.* 0.25 – 0.4 V) overpotentials. While the exact underlying mechanism of this observation is still under debate, multiple Tafel slopes have been observed for other OER catalysts, and it is likely related to a change in intermediate surface coverage with increasing electrode potential (62). Therefore, the Tafel slope and kinetic parameters at both low and higher overpotentials are reported and discussed.

[Insert Figure 4]

Table 3. Summary of Electrokinetic Parameters from iR Corrected LSVs fit to Tafel Equation

	Low η Region			High η Region		
	Tafel Slope/mV			Tafel Slope/mV		
Sample	dec^{-1}	α	j_0/mA cm^{-1}	dec^{-1}	α	j_0/mA cm^{-2}
Ni Foam	63	0.44	2.50	134	0.21	0.33
PC-TM-25	77	0.36	0.34	130	0.21	0.11
PC-MP-25	62	0.45	1.44	127	0.22	0.21
PC-TM-100	78	0.36	0.17	134	0.21	0.07
PC-MP-100	74	0.38	0.23	97	0.29	0.12
PE-TM-100	58	0.48	0.77	126	0.22	0.11
PE-MP-100	73	0.38	0.22	117	0.24	0.08

PC-MP-25 shows an improvement in kinetics compared to PC-TM-25 in regard to Tafel slope at low η (62 vs. 77 mV dec^{-1}) and slightly at high η (127 vs. 130 mV dec^{-1}). The change in Tafel slope from low to high overpotential can be due to changes in the rate determining step (RDS) and/or changes in the surface composition of adsorbed species (61, 63). It has been reported that observing a second Tafel slope at higher overpotential of ~120 mV/dec is typically due to a build-up of surface species formed in the step just prior to the RDS (61), where the reaction rate becomes exponentially dependent on the applied potential (62). The Tafel slope can be used to predict the RDS in the OER mechanism. Although the OER mechanism is complex and debated (64), assuming a single-site mechanism, it may proceed via the following steps (61):

$$M + OH^- \rightleftharpoons M\text{-}OH + e^- \quad (8)$$

$$M\text{-}OH + OH^- \rightleftharpoons M\text{-}O + H_2O + e^- \quad (9)$$

$$M\text{-}O + OH^- \rightleftharpoons M\text{-}OOH + e^- \quad (10)$$

$$M\text{-}OOH + OH^- \rightleftharpoons M\text{-}OO^- + H_2O \quad (11)$$

$$M\text{-}OO^- \rightleftharpoons M + O_2 + e^- \quad (12)$$

Each RDS possesses a unique Tafel slope that can be calculated from the Tafel equation (Eq. (7)) based on the number of electron transfers (n) that occur prior to the RDS (65). Assuming a perfectly reversible reaction (α = 0.5) at T = 50 °C, the Tafel slope if the RDS were Eq. (8), the first electron transfer step where n = 0, would be ~128 mV dec. If the RDS were Eq. (9) or (10), Tafel slopes of ~43 or ~26 mV dec^{-1} would be predicted, respectively. Alternatively, if the RDS is the initial adsorption of OH^- while the subsequent electron transfer is more facile, a Tafel slope of 64 mV dec^{-1} (or 60 mV dec^{-1} at 30 °C (62, 65)) is calculated. Considering the Tafel slopes for PC-TM-25 and PC-MP-25 are 77 and 62 mV dec^{-1} respectively, the RDS is most likely the initial

adsorption of OH^-, which is comparatively faster for PC-MP-25 than PC-TM-25. Similar Tafel slopes have been reported for other Ni-based catalysts in alkaline media (10, 66-68).

The charge transfer coefficient (α) for PC-MP-25 is also comparatively higher (0.45 vs. 0.35) and close to 0.5, indicating the OER reaction shows nearly reversible behavior. Marcus theory describes a model for an outer-sphere single electron charge transfer where both the reactant and product do not interact directly with the electrode surface (69). In Marcus theory, α, the charge transfer coefficient, is described by Eq. (13) as a function of η, the overpotential, and λ, the reorganization energy required to transform the nuclear configuration of the reactant to the product.

$$\alpha = \frac{1}{2}\left(1 + \frac{\eta F}{\lambda}\right) \qquad (13)$$

From Eq. (13), when $\lambda >> \eta F$, $\alpha \rightarrow 0.5$, indicating a perfectly reversible reaction. α will deviate from 0.5 when either λ is lowered or at higher η in the Tafel region. λ can decrease when reactions occur with a reactant adsorbed to a surface, which decreases solvent effects by eliminating part of the solvation shell, or by shortening the distance between the reactant and electrode (70). Therefore, PC-TM-25 may exhibit a lower α, which deviates more significantly from 0.5, because of detrimental effects between the catalyst interface and TMA moieties.

Table 4. Summary of OER Performance Parameters from iR Corrected LSVs

Sample	Onset Potential/V	η_{10}/ mV	η_{100}/ mV	j @ 1.75 V/mA cm^{-2}	Mass Activity @ 1.75 V /A g^{-1}	C_{dl} /mF cm^{-2}
Ni Foam	1.59	210	n/a	30	n/a	1.4
PC-TM-25	1.51	100	290	90	35	12.5
PC-MP-25	1.57	170	380	54	21	8.0
PC-TM-100	1.46	60	260	128	80	12.4
PC-MP-100	1.48	60	250	140	88	8.8
PE-TM-100	1.54	119	288	103	64	12.1
PE-MP-100	1.54	69	226	187	117	20.8

Additional performance parameters for all electrodes investigated in this work are provided in Table 4 (and for results from LSVs without iR correction, in Table S4). PC-MP-25 displays a much larger exchange current density than PC-TM-25 and approaches that of the pristine Ni foam. As exchange current density is a measure of the intrinsic electron transfer rate, this result further demonstrates the superior kinetics afforded by the MPRD cationic moiety. Despite this, PC-TM-25 ultimately displayed better performance, having a slightly lower onset potential, a lower overpotential at both 10 and 100 mA cm^{-2} (η_{10} and η_{100}), and a higher j and mass activity @ 1.75 V. To investigate this further, the double layer capacitance (C_{dl}) was also determined from cyclic voltammetry (CV) at scan rates of 10, 20, 30 and 50 mV s^{-1} between 1.12 and 1.22 V (see Figure S8 for all CV scans). C_{dl} is directly proportional to the electrochemical surface area (ECSA) and can be used as a representation of that when comparing similar samples. Notably,

upon adding any Ag-ionomer ink to the Ni foam, C_{dl} increases substantially due to the addition of Ag nanoparticles. The effect of the QAC is also substantial on C_{dl}, where PC-TM-25 shows a larger C_{dl} than PC-MP-25 (12.5 vs 8.0 mF cm^{-2}) and therefore possesses a larger ECSA. PC-TM-25 possessing a higher ECSA is counterintuitive, considering charge transfer is typically promoted with a higher availability of active sites (71). Nonetheless, while OER is promoted for PC-MP-25, shown by faster kinetics and a higher α, PC-TM-25 shows better performance due to possessing a larger active catalyst surface area. The larger active area and more favorable electrode structure provided by the TMA moiety to impart enhanced OER performance could be due to electrostatic interactions between the TMA moiety and the Ag or Ni surface, though further investigations using DFT are necessary to support this hypothesis.

3.2.2 Comparison of Ink Dilution

Next, the effect of ink dilution was investigated. The mass ratio of solid:liquid was increased from 1:25 to 1:100 to make PC-TM-100 and PC-MP-100. The catalyst loading was also reduced from 2.6 to 1.6 mg cm^{-2}, keeping the same I:C ratio. The LSVs for PC-TMA-100 and PC-MPRD-100 can be seen in Figure 5.

[Insert Figure 5]

Ink dilution did not have a substantial effect on the OER kinetics of the PC-TM electrodes. Dilution led to a slight increase in the Tafel slope in both the low and high current density regions. A slight decrease in j_0 (0.34 vs. 0.17 mA cm^{-2}) is also noted. Additionally, only small variations in C_{dl} were observed with ink dilution for both PC-TM-100 and PC-MPRD-100. Despite minor effects on the kinetics, a more significant decrease in η_{10} and η_{100}, and a higher j and mass activity @ 1.75 V are seen with dilution. Decreasing the ionomer thickness is also

known to decrease mass transport resistance to and from the catalyst surface, thereby enhancing performance.

Ink dilution had a more substantial effect on the OER kinetics of the PC-MP electrodes. At low current densities, the Tafel slope at low η increased with ink dilution from 62 for PC-MP-25 to 74 mV dec^{-1} for PC-MP-100. However, at higher overpotentials, the Tafel slope decreased considerably to 97 mV dec^{-1}, giving PC-MP-100 a lower Tafel slope than PC-MP-25, PC-TM-25 and PC-TM-100. A Tafel slope of 97 mV dec^{-1} also indicates the reaction kinetics are not yet limited by the surface coverage of adsorbed OH (M-OH), which would result in a Tafel slope closer to 128 mV dec^{-1} at 50 °C. Instead, the initial adsorption of OH^- is still the RDS at higher overpotentials, just with comparatively slower kinetics. Ultimately, this manifests in lower overpotentials at higher current densities for PC-MP-100. Additionally, the exchange current density decreases with ink dilution, with the MPRD-functionalized ionomer ink still possessing higher intrinsic charge transfer. Kinetics aside, the overall performance of PC-TM-100 and PC-MP-100 is similar. The most significant enhancements with ink dilution can be observed in mass activity (normalized /g Ag), which greatly improved with ink dilution as shown in Figure 6 (see Figure S12 for mass activity plot with no iR correction). This indicates catalyst utilization was greatly improved by diluting the catalyst ink, which effectively decreases the ionomer thickness on the Ag catalyst particles and Ni foam support. Major differences between TMA and MPRD observed in more concentrated inks are less pronounced in diluted inks. Mainly, the change in the RDS for PC-MP-100 at high overpotential indicates the interface between the catalyst surface and MPRD moiety limits the build-up of intermediates and provides an overall promotion of the OER reaction.

[Insert Figure 6]

3.2.3 Comparison of Partial Hydrogenation at Ni Foam Interface

For nearly a century the efficacy of Ni and Ni-based catalysts for facilitating hydrogenation reactions has been demonstrated in a variety of applications (72, 73) including the hydrogenation of nitriles (74), *n*-butyraldehyde and acetone (75), internal alkyne-containing nitroarene (76), and polybutadiene to polyethylene (77). Therefore, in this work, the authors leveraged the catalytic properties of the Ni foam substrate to partially hydrogenate the triblock block copolymer PCMS-*b*-PCOE-*b*-PCMS coating to PCMS-*b*-PE-*b*-PCMS (see section **2.4** for detailed procedure).

The characterization of the hydrogenated block copolymer on Ni foam proved challenging with spectroscopic techniques including FTIR, where adequate intensity of the thin film was difficult to obtain using ATR-FTIR, and Raman (where only broad amorphous carbon peaks were observed, likely due to laser-induced Ag nanoparticle-catalyzed degradation (78)). Therefore, differential scanning calorimetry (DSC) was used to identify changes in the melting point, where PCOE melts near ~ 55 °C and PE near ~130 °C. For DSC, a small (~1 cm^2) piece of Ni foam was coated in 1.3 mg of the PCMS-*b*-PCOE-*b*-PCMS triblock copolymer precursor and hydrogenated in H_2. While this was nearly ~4x the polymer loading used in experiments, the DSC experiment was limited by the volume of Ni foam that could fit in the pan and mass of polymer required to obtain an adequate heat flow signal. The DSC curves can be viewed in Figure S13. It is clear PCOE is still present in the sample, but there is partial hydrogenation noted by the small deviation near the melting point of PE. It is likely the Ni foam was only able to hydrogenate the block copolymer at the Ni foam interface, while the rest of the polymer remained unsaturated. A larger ratio of the block copolymer would be hydrogenated with the polymer loadings utilized on the electrodes in this work. Therefore, the effect of partially hydrogenating the ionomer was still investigated, as PE can offer enhanced properties compared to PCOE (79, 80), most notably

reduced water uptake and swelling (41), which is critical for water management in AEMWEs (31, 32, 81-83).

[Insert Figure 7]

Further evidence of the partial hydrogenation of the ionomer at the Ni-foam interface is shown in the substantial effect on the OER kinetics and performance of both PE-TM-100 and PE-MP-100 electrodes (Figure 7). For PE-TM-100, partial hydrogenation led to a decrease in the Tafel slope in both the low and high current density regions, an increase in α, and an increase in j_0 (from 0.17 to 0.77 mA cm^{-2}). The decrease in the Tafel slope from 78 to 58 mV dec^{-1} indicates the kinetics of OER are much faster after hydrogenating the ionomer at the Ni foam interface. Further, charge transfer is clearly improved, as noted by the increase in j_0 and α = 0.48. This behavior indicates nearly reversible, facile kinetic behavior. For PC-MP-100, the kinetics are essentially unchanged except for a higher Tafel slope at high η near 117 mV dec^{-1}. The Tafel slope being this far below the predicted slope for the RDS being the first electron transfer (128 mV dec^{-1}) indicates the mechanism is likely the same as on PC-MP-100, where the reaction kinetics are not yet limited by the surface coverage of adsorbed OH (M-OH) and the initial adsorption of OH^- is still the RDS at higher overpotentials. This phenomenon, which enhanced the performance of PC-MP-100 beyond PC-TM-100, also improves the performance of PE-MP-100 beyond that of PC-TM-100. It also affords PE-MP-100 a lower η_{10} than PE-TM-100, in addition to the lowest η_{100} and the higher j and mass activity @ 1.75 V of any catalyst ink investigated in this work. The mass activity of PE-TM-100 and PE-MP-100 can also be viewed in Figure 6.

In addition to the RDS at high overpotentials, the ECSA had a substantial effect on enhancing the performance of the PE-MP-100 electrode. While the C_{dl} of PE-TM-100 remained relatively

consistent after partial hydrogenation, the C_{dl} of PE-MP-100 was significantly enhanced after partial hydrogenation, increasing from 8.8 mF cm^{-2} for PC-MP-100 to 20.8 mF cm^{-2} for PE-MP-100. This > 2-fold increase in C_{dl}, and therefore ECSA, resulted in a greater OER performance enhancement. The highest performing electrode is therefore PE-MP-100. The mechanistic reason for the improvement in ECSA could be due to complex interactions between the partially hydrogenated PE backbone and the MPRD moiety, however further studies beyond the scope of this work will be necessary to fully evaluate this phenomenon.

3.3 Performance Demonstration in AEM electrolyzer

3.3.1 AEM Characterization

The Tuffbrane™ polymer is one commercial iteration of a triblock copolymer published previously (41) of the same chemistry with a different composition, as described in the supplemental information. The AEMs were fabricated in-house with a thickness of 38 ± 5 μm with an IEC of 0.64 ± 0.04 mmol g^{-1}. The ionic conductivity and morphology of the AEM were characterized in aqueous conditions relevant to the electrolysis tests. Conductivity in the Cl^- and CO_3^{2-} form was determined using EIS at both 25 and 50 °C and is summarized in Table S4. SAXS was performed on dry and H_2O immersed membranes (Figure S14). The domain spacing (d-spacing) was calculated from the primary q^* peak. D-spacing of the membrane increased from 33.7 to 36.1 nm with hydration in liquid water due to swelling of the hydrophilic domains. The secondary peak is located at ~2q, indicating a lamellar morphology (84). Additionally, the Porod slope is close to 2 (shown in Figure S14), indicating a particle symmetry of lamellar domains in agreement with the ratio of q values at each peak (85).

3.3.2 AEM Electrolyzer Performance

The optimized OER anode, PE-MP-100, along with PE-TM-100, were demonstrated in an AEM electrolyzer to correlate the results from the half-cell study to an operating device (86, 87). Membrane electrode assemblies (MEAs) were prepared using PE-TM-100 or PE-MP-100 anodes as described in section **2.7**. The electrolyzer with the PE-TM-100 or PE-MP-100 anode will be refered to as EL-PE-TM and EL-PE-MP, respectively. Polarization curves were collected at 50 °C in both 1 M K_2CO_3 and DI water (see Figure 8). iR correction was performed by evaluating the high-frequency resistance (HFR) from EIS measurements (see Figure S15). The area specific resistances (ASRs) of the EL-PE-TM and EL-PE-MP electrolyzers are summarized in Table 5. Raw polarization curves can be view in Figure S16.

Table 5. Area Specific Resistances (ASR) of AEM Electrolyzers in 1 M K_2CO_3 and DI H_2O

Electrolyzer	Feed Liquid	ASR/ ohm cm^2
EL-PE-MP	1 M K_2CO_3	0.62
	DI H_2O	2.10
EL-PE-TM	1 M K_2CO_3	0.74
	DI H_2O	4.50

Figure 8 shows that EL-PE-MP maintains superior performance over EL-PE-TM. In 1 M K_2CO_3, the EL-PE-MP cell achieved a performance of 1 A cm^{-2} at 2.20 V. This is further corroborated by the ASR, which is slightly higher for EL-PE-TM due to TMA cationic functionality. The performance gap between the two anodes is emphasized in DI H_2O. Performance was significantly reduced in both cells, with EL-PE-TM only reaching a current density of 40 mA cm^{-2} at 2.92 V and EL-PE-MP reaching a current density of 120 mA cm^{-2} at 2.74 V. The ASR also substantially increases in DI H_2O due to the removal of circiculating electrolyte, and EL-PE-

TM has an ASR more than double that of EL-PE-MP. Poorer performance in AEM water electrolyzers is attributed to a lowering of the pH and degradation in catalyst activity as a result. Developing effective catalysts for OER in neutral pH still remains a challenge in the field (88).

[Insert Figure 8]

Diagnosing device durability to achieve a practical device is a complex and time consuming task (83). However, the durability of this first iteration of the EL-PE-MP electrolyzer was assessed by applying a constant current of 500 mA cm^{-2} for 5 h (see Figure 9), as a baseline. Over the course of the experiment, the cell voltage decreased, indicative of either a soft short, H_2 cross-over, or membrane thinning, though this type of degradation mechanism is challenging to diagnose (83). Future necessary work will include optimization of the MEA components and assembly of the cell, including the hardware, gaskets, sealing pressure and flow rates is expected to result in dramatic improvements in performance and durability.

[Insert Figure 9]

4. Conclusions

The OER performance of a series of Ag-ionomer catalyst inks on Ni foam are evaluated in half-cell experiments. Different ionomer modifications are investigated to optimize the OER performance. First, the block copolymer precursor PCMS-*b*-PCOE-*b*-PCMS is functionalized with either benzyltrimethylammonium or benzylmethylpiperidinium quaternary ammonium cations. While the MPRD-functionalized ionomer facilitates enhanced OER kinetics, the TMA-functionalized ionomer ultimately has better performance likely due to exhibiting a larger ECSA. Both catalyst inks were subsequently diluted and their catalyst loading was reduced while keeping the same I:C ratio. Ink dilution had a negligible effect on the kinetics of the TMA-

functionalized ionomer. In constrast, diluting the MPRD-functionalized ionomer catalyst ink enabled the RDS at higher overpotentials to be the initial adsorption of OH (indicated by a Tafel slope of 97 mV dec^{-1}). Comparatively, all TMA-functionalized ionomer catalyst inks were limited by the surface coverage of adsorbed OH (M-OH) and the first electron transfer at high overpotentials (indicated by a Tafel slopes > 128 mV dec^{-1}). Overall, ink dilution also enhanced the performance and catalyst utilization in both samples likely by reducing transport resistances via decreasing the ionomer thickness on the Ag catalyst particles and Ni foam support.

The catalytic activity of the Ni foam support was leveraged to partially hydrogenate the deposited PCMS-*b*-PCOE-*b*-PCMS block copolymer midblock to polyethylene (PE). After functionalization with MPRD, this variation of the electrode displayed further enhancements in performance, likely due to the enhanced properties of PE compared to PCOE. The same enhanced kinetics at higher overpotentials were also observed. Interestingly, a large enhancement in the ECSA was observed only in the MPRD-functionalized ink, which likely played a role in the observed performance enhancement. Overall, MPRD cationic moieties consistently provided lower Tafel slopes and higher charger transfer coefficients at high overpotentials, which ultimately had a larger impact on the overall performance than the Tafel slope and kinetics observed at lower overpotentials. This originated from a shift in the RDS at high overpotentials, which was only observed in MPRD-functionalized catalyst ink samples, where the OER reaction rate was not limited by the build-up of surface intermediates. Finally, the performance of the optimized electrode PE-MP-100 was compared to PE-TM-100 in an AEM electrolyzer operating at 50 °C in both 1 M K_2CO_3 and DI H_2O. The performance observations from the half-cell experiments correlated well to single-cell performance, with PE-MP-100 significantly outperforming PE-TM-100 in both achievable current density and

operating at lower cell voltages. The degradation behavior of the AEM electrolyzer indicates that further optimization of the cell assembly or membrane are required to realize further performance improvements.

Acknowledgements

The authors gratefully acknowledge the financial support from the Army Research Office through Grants W911NF-17-1-0568 and W911NF-19-1-0286. This research used resources of the Advanced Photon Source, a U.S. Department of Energy (DOE) Office of Science User Facility, operated for the DOE Office of Science by Argonne National Laboratory under Contract No. DE-AC02-06CH11357. The authors acknowledge useful discussions with Dr. Nemanja Danilovic, Lawrence Berkeley National Laboratory.

Appendices

See attached Supporting Information for Publication.

References

1. Ruth MF, Jadun P, Gilroy N, Connelly E, Boardman R, Simon AJ, et al. The Technical and Economic Potential of the H2@Scale Concept within the United States. National Renewable Energy Laboratory; 2020. Contract No.: NREL/TP-6A20-77610.
2. Ayers K, Danilovic N, Ouimet R, Carmo M, Pivovar B, Bornstein M. Perspectives on Low-Temperature Electrolysis and Potential for Renewable Hydrogen at Scale. Annual Review of Chemical and Biomolecular Engineering. 2019;10(1):219-39.
3. Saba SM, Müller M, Robinius M, Stolten D. The investment costs of electrolysis – A comparison of cost studies from the past 30 years. Int J Hydrogen Energy. 2018;43(3):1209-23.
4. Pavel CC, Cecconi F, Emiliani C, Santiccioli S, Scaffidi A, Catanorchi S, et al. Highly Efficient Platinum Group Metal Free Based Membrane-Electrode Assembly for Anion Exchange Membrane Water Electrolysis. Angew Chem, Int Ed. 2014;53(5):1378-81.
5. Ahn SH, Lee B-S, Choi I, Yoo SJ, Kim H-J, Cho E, et al. Development of a membrane electrode assembly for alkaline water electrolysis by direct electrodeposition of nickel on carbon papers. Applied Catalysis B: Environmental. 2014;154-155:197-205.
6. Vincent I, Bessarabov D. Low cost hydrogen production by anion exchange membrane electrolysis: A review. Renewable Sustainable Energy Rev. 2018;81:1690-704.

7. Zeng L, Zhao TS. Integrated inorganic membrane electrode assembly with layered double hydroxides as ionic conductors for anion exchange membrane water electrolysis. Nano Energy. 2015;11:110-8.
8. Chen P, Xu K, Zhou T, Tong Y, Wu J, Cheng H, et al. Strong-Coupled Cobalt Borate Nanosheets/Graphene Hybrid as Electrocatalyst for Water Oxidation Under Both Alkaline and Neutral Conditions. Angew Chem, Int Ed. 2016;55(7):2488-92.
9. Nie Z-P, Ma D-K, Fang G-Y, Chen W, Huang S-M. Concave Bi2WO6 nanoplates with oxygen vacancies achieving enhanced electrocatalytic oxygen evolution in near-neutral water. J Mater Chem A. 2016;4(7):2438-44.
10. Sun Y, Liu C, Zhang L, Wan P, Zhuang S, Tang Y, et al. Ultrafast Electrodeposition of Ni−Fe Hydroxide Nanosheets on Nickel Foam as Oxygen Evolution Anode for Energy-Saving Electrolysis of Na2CO3/NaHCO3. ChemElectroChem. 2017;4(5):1044-50.
11. Ito H, Kawaguchi N, Someya S, Munakata T, Miyazaki N, Ishida M, et al. Experimental investigation of electrolytic solution for anion exchange membrane water electrolysis. Int J Hydrogen Energy. 2018;43(36):17030-9.
12. Liu J, Kang Z, Li D, Pak M, Alia SM, Fujimoto C, et al. Elucidating the Role of Hydroxide Electrolyte on Anion-Exchange-Membrane Water Electrolyzer Performance. J Electrochem Soc. 2021;168(5):054522.
13. Cao X, Novitski D, Holdcroft S. Visualization of Hydroxide Ion Formation upon Electrolytic Water Splitting in an Anion Exchange Membrane. ACS Materials Letters. 2019;1(3):362-6.
14. Ziv N, Dekel DR. A practical method for measuring the true hydroxide conductivity of anion exchange membranes. Electrochem Commun. 2018.
15. Krewer U, Weinzierl C, Ziv N, Dekel DR. Impact of carbonation processes in anion exchange membrane fuel cells. Electrochim Acta. 2018;263:433-46.
16. John SS, Atkinson RW, Roy A, Unocic RR, Papandrew AB, Zawodzinski TA. The Effect of Carbonate and pH on Hydrogen Oxidation and Oxygen Reduction on Pt-Based Electrocatalysts in Alkaline Media. J Electrochem Soc. 2016;163(3):F291-F5.
17. Doan H, Malley J, Jankins T, Lin C, Primbetova A, Mukerjee S, editors. Catalytic and Mass Transport Effects of Carbonate Ions at an Anion Exchange Membrane Interface (PGM vs. non-PGM) for a Practical and Efficient Water Splitting Cell. ECS Meeting Abstracts; 2017: The Electrochemical Society.
18. Stucki S, Schuler A, Constantinescu M. Coupled CO2 recovery from the atmosphere and water electrolysis: Feasibility of a new process for hydrogen storage. Int J Hydrogen Energy. 1995;20(8):653-63.
19. Poojary S, Islam MN, Shrivastava UN, Roberts EPL, Karan K. Transport and Electrochemical Interface Properties of Ionomers in Low-Pt Loading Catalyst Layers: Effect of Ionomer Equivalent Weight and Relative Humidity. Molecules (Basel, Switzerland). 2020;25(15):3387.
20. Ohma A, Fushinobu K, Okazaki K. Influence of Nafion® film on oxygen reduction reaction and hydrogen peroxide formation on Pt electrode for proton exchange membrane fuel cell. Electrochimica Acta. 2010;55(28):8829-38.
21. Visser SP. Second-Coordination Sphere Effects on Selectivity and Specificity of Heme and Nonheme Iron Enzymes. Chemistry A European Journal. 2020;26(24):5308-27.
22. Fu Q, Bao X. Confined microenvironment for catalysis control. Nature Catalysis. 2019;2(10):834-6.
23. Koshy DM, Akhade SA, Shugar A, Abiose K, Shi J, Liang S, et al. Chemical Modifications of Ag Catalyst Surfaces with Imidazolium Ionomers Modulate H2 Evolution Rates during Electrochemical CO2 Reduction. Journal of the American Chemical Society. 2021;143(36):14712-25.
24. McCrum IT, Hickner MA, Janik MJ. Quaternary Ammonium Cation Specific Adsorption on Platinum Electrodes: A Combined Experimental and Density Functional Theory Study. J Electrochem Soc. 2018;165(2):F114-F21.

25. Maurya S, Dumont JH, Villarrubia CN, Matanovic I, Li D, Kim YS, et al. Surface Adsorption Affects the Performance of Alkaline Anion-Exchange Membrane Fuel Cells. ACS Catalysis. 2018;8(10):9429-39.
26. Kodama K, Motobayashi K, Shinohara A, Hasegawa N, Kudo K, Jinnouchi R, et al. Effect of the Side-Chain Structure of Perfluoro-Sulfonic Acid Ionomers on the Oxygen Reduction Reaction on the Surface of Pt. ACS Catalysis. 2018.
27. Park EJ, Maurya S, Lee AS, Leonard DP, Li D, Jeon JY, et al. How does a small structural change of anode ionomer make a big difference in alkaline membrane fuel cell performance? J Mater Chem A. 2019;7(43):25040-6.
28. Martens S, Asen L, Ercolano G, Dionigi F, Zalitis C, Hawkins A, et al. A comparison of rotating disc electrode, floating electrode technique and membrane electrode assembly measurements for catalyst testing. J Power Sources. 2018;392:274-84.
29. Kwan JTH, Bonakdarpour A, Afonso G, Wilkinson DP. Bridging Fundamental Electrochemistry with Applied Fuel Cell Testing: A Novel and Economical Rotating Disk Electrode Tip for Electrochemical Assessment of Catalyst-Coated Membranes. Electrochim Acta. 2017;258:208-19.
30. Ghoshal S, Pivovar BS, Alia SM. Evaluating the effect of membrane-ionomer combinations and supporting electrolytes on the performance of cobalt nanoparticle anodes in anion exchange membrane electrolyzers. J Power Sources. 2021;488:229433.
31. Huang G, Mandal M, Hassan NU, Groenhout K, Dobbs A, Mustain WE, et al. Ionomer Optimization for Water Uptake and Swelling in Anion Exchange Membrane Electrolyzer: Oxygen Evolution Electrode. J Electrochem Soc. 2020;167:164514.
32. Huang G, Mandal M, Hassan NU, Groenhout K, Dobbs A, Mustain WE, et al. Ionomer Optimization for Water Uptake and Swelling in Anion Exchange Membrane Electrolyzer: Hydrogen Evolution Electrode. J Electrochem Soc. 2021;168:024503.
33. Faid AY, Xie L, Barnett AO, Seland F, Kirk D, Sunde S. Effect of anion exchange ionomer content on electrode performance in AEM water electrolysis. Int J Hydrogen Energy. 2020;45(53):28272-84.
34. Loukrakpam R, Ferreira Gomes B, Kottakkat T, Roth C. A bird's eye perspective of the measurement of oxygen reduction reaction in gas diffusion electrode half-cell set-ups for Pt electrocatalysts in acidic media. Journal of Physics: Materials. 2021;4(4):044004.
35. Mardle P, Thirunavukkarasu G, Guan S, Chiu Y-L, Du S. Comparative Study of PtNi Nanowire Array Electrodes toward Oxygen Reduction Reaction by Half-Cell Measurement and PEMFC Test. ACS Appl Mater Interfaces. 2020;12(38):42832-41.
36. Dembinska B, Zlotorowicz A, Modzelewska M, Miecznikowski K, Rutkowska IA, Stobinski L, et al. Low-Noble-Metal-Loading Hybrid Catalytic System for Oxygen Reduction Utilizing Reduced-Graphene-Oxide-Supported Platinum Aligned with Carbon-Nanotube-Supported Iridium. Catalysts. 2020;10(6).
37. Franzen D, Ellendorff B, Paulisch MC, Hilger A, Osenberg M, Manke I, et al. Influence of binder content in silver-based gas diffusion electrodes on pore system and electrochemical performance. J Appl Electrochem. 2019;49(7):705-13.
38. Bogolowski N, Ngaleu O, Sakthivel M, Drillet JF. Long-life bifunctional BaSrCoFeO3/C gas diffusion electrode. Carbon. 2017;119:511-8.
39. Sapountzi FM, Orlova ED, Sousa JPS, Salonen LM, Lebedev OI, Zafeiropoulos G, et al. FeP Nanocatalyst with Preferential [010] Orientation Boosts the Hydrogen Evolution Reaction in Polymer-Electrolyte Membrane Electrolyzer. Energy & Fuels. 2020;34(5):6423-9.
40. Liu Y, Pandey TP, Sarode HN, Kuo MC, Zhang W, Gupta R, et al. Thin, robust, and chemically stable photo-cross-linked anion exchange membranes based on a polychlorostyrene-b-polycyclooctene-b-polychlorostyrene ABA triblock polymer. Solid State Ionics. 2018;316:135-42.
41. Buggy NC, Du Y, Kuo MC, Ahrens KA, Wilkinson JS, Seifert S, et al. A Polyethylene-Based Triblock Copolymer Anion Exchange Membrane with High Conductivity and Practical Mechanical Properties. ACS Appl Polym Mater. 2020;2(3):1294-303.

42. Banhart J. Manufacture, characterisation and application of cellular metals and metal foams. Prog Mater Sci. 2001;46(6):559-632.
43. Han G-Q, Liu Y-R, Hu W-H, Dong B, Li X, Shang X, et al. Three dimensional nickel oxides/nickel structure by in situ electro-oxidation of nickel foam as robust electrocatalyst for oxygen evolution reaction. Appl Surf Sci. 2015;359:172-6.
44. Yan K-L, Shang X, Gao W-K, Dong B, Li X, Chi J-Q, et al. Ternary MnO2/NiCo2O4/NF with hierarchical structure and synergistic interaction as efficient electrocatalysts for oxygen evolution reaction. J Alloys Compd. 2017;719:314-21.
45. van Drunen J, Pilapil BK, Makonnen Y, Beauchemin D, Gates BD, Jerkiewicz G. Electrochemically Active Nickel Foams as Support Materials for Nanoscopic Platinum Electrocatalysts. ACS Appl Mater Interfaces. 2014;6(15):12046-61.
46. Sivanantham A, Shanmugam S. Nickel selenide supported on nickel foam as an efficient and durable non-precious electrocatalyst for the alkaline water electrolysis. Applied Catalysis B: Environmental. 2017;203:485-93.
47. Pierozynski B, Mikolajczyk T, Luba M, Zolfaghari A. Kinetics of oxygen evolution reaction on nickel foam and platinum-modified nickel foam materials in alkaline solution. Journal of Electroanalytical Chemistry. 2019;847:113194.
48. Li C, Chen J, Wu Y, Cao W, Sang S, Wu Q, et al. Enhanced oxygen evolution reaction activity of NiFe layered double hydroxide on nickel foam- reduced graphene oxide interfaces. Int J Hydrogen Energy. 2019;44(5):2656-63.
49. Vij V, Sultan S, Harzandi AM, Meena A, Tiwari JN, Lee WG, et al. Nickel-Based Electrocatalysts for Energy-Related Applications: Oxygen Reduction, Oxygen Evolution, and Hydrogen Evolution Reactions. ACS Catalysis. 2017;7(10):7196-225.
50. Chen YP, Rui K, Zhu JX, Dou SX, Sun WP. Recent Progress on Nickel-Based Oxide/(Oxy)Hydroxide Electrocatalysts for the Oxygen Evolution Reaction. Chem Eur J. 2019;25(3):703-13.
51. Buggy NC, Du Y, Kuo M-C, Gasvoda RJ, Seifert S, Agarwal S, et al. Investigating Silver Nanoparticle Interactions with Quaternary Ammonium Functionalized Triblock Copolymers and Their Effect on Midblock Crystallinity. ACS Appl Polym Mater. 2020;2(11):4914-23.
52. Buggy NC, Du Y, Kuo M-C, Seifert S, Gasvoda RJ, Agarwal S, et al. Designing Anion-Exchange Ionomers with Oriented Nanoscale Phase Separation at a Silver Interface. The Journal of Physical Chemistry C. 2021;125(37):20592-605.
53. Zhang W. Synthesis and Characterization of Polymeric Anion Exchange Membranes. Ph.D. Thesis: University of Massachusetts Amherst; 2016.
54. Tsai TH, Ertem SP, Maes AM, Seifert S, Herring AM, Coughlin EB. Thermally cross-linked anion exchange membranes from solvent processable isoprene containing ionomers. Macromolecules. 2015.
55. Sing KSW. 7 - Assessment of Surface Area by Gas Adsorption. In: Rouquerol F, Rouquerol J, Sing KSW, Llewellyn P, Maurin G, editors. Adsorption by Powders and Porous Solids (Second Edition). Oxford: Academic Press; 2014. p. 237-68.
56. Hansen HA, Rossmeisl J, Nørskov JK. Surface Pourbaix diagrams and oxygen reduction activity of Pt, Ag and Ni(111) surfaces studied by DFT. Physical Chemistry Chemical Physics. 2008;10(25):3722-30 , ISSN = 1463-9076 , DOI = 10.1039/B803956A.
57. Medway SL, Lucas CA, Kowal A, Nichols RJ, Johnson D. In situ studies of the oxidation of nickel electrodes in alkaline solution. Journal of Electroanalytical Chemistry. 2006;587(1):172-81.
58. Bard AJ, Faulkner LR. Electrochemical Methods: Fundamentals and Applications, 2nd Edition. New York: John Wiley & Sons, Inc.; 2000.
59. Ertem SP, Tsai TH, Donahue MM, Zhang W, Sarode H, Liu Y, et al. Photo-Cross-Linked Anion Exchange Membranes with Improved Water Management and Conductivity. Macromolecules. 2016;49(1):153-61.

60. Zheng W, Liu M, Lee LYS. Best Practices in Using Foam-Type Electrodes for Electrocatalytic Performance Benchmark. ACS Energy Lett. 2020;5(10):3260-4.
61. Shinagawa T, Garcia-Esparza AT, Takanabe K. Insight on Tafel slopes from a microkinetic analysis of aqueous electrocatalysis for energy conversion. Scientific Reports. 2015;5(1):13801.
62. Zhang J, Tao HB, Kuang M, Yang HB, Cai W, Yan Q, et al. Advances in Thermodynamic-Kinetic Model for Analyzing the Oxygen Evolution Reaction. ACS Catalysis. 2020;10(15):8597-610.
63. Ponce J, Rehspringer JL, Poillerat G, Gautier JL. Electrochemical study of nickel–aluminium–manganese spinel NixAl1−xMn2O4. Electrocatalytical properties for the oxygen evolution reaction and oxygen reduction reaction in alkaline media. Electrochim Acta. 2001;46(22):3373-80.
64. Conway BE, Tilak BV. Behavior and Characterization of Kinetically Involved Chemisorbed Intermediates in Electrocatalysis of Gas Evolution Reactions. In: Eley DD, Pines H, Weisz PB, editors. Advances in Catalysis. 38: Academic Press; 1992. p. 1-147.
65. Fang Y-H, Liu Z-P. Tafel Kinetics of Electrocatalytic Reactions: From Experiment to First-Principles. ACS Catalysis. 2014;4(12):4364-76.
66. Iqbal MZ, Kriek RJ. Silver/Nickel Oxide (Ag/NiO) Nanocomposites Produced Via a Citrate Sol-Gel Route as Electrocatalyst for the Oxygen Evolution Reaction (OER) in Alkaline Medium. Electrocatalysis. 2018;9(3):279-86.
67. Masa J, Barwe S, Andronescu C, Sinev I, Ruff A, Jayaramulu K, et al. Low Overpotential Water Splitting Using Cobalt–Cobalt Phosphide Nanoparticles Supported on Nickel Foam. ACS Energy Lett. 2016;1(6):1192-8.
68. Zhang C, Xie Z, Liang Y, Meng D, Wang Z, He X, et al. Morphological and compositional modification of β-Ni(OH)2 nanoplates by ferrihydrite for enhanced oxygen evolution reaction. Int J Hydrogen Energy. 2021;46(34):17720-30.
69. Marcus RA. Chemical and Electrochemical Electron-Transfer Theory. Annu Rev Phys Chem. 1964;15(1):155-96.
70. Schmickler W, Santos E. Interfacial Electrochemistry, 2nd Edition. London, New York: Springer-Verlag Berlin Heidelberg; 2010.
71. Kou T, Wang S, Hauser JL, Chen M, Oliver SRJ, Ye Y, et al. Ni Foam-Supported Fe-Doped β-Ni(OH)2 Nanosheets Show Ultralow Overpotential for Oxygen Evolution Reaction. ACS Energy Lett. 2019;4(3):622-8.
72. Adkins H, Cramer HI. The use of nickel as a catalyst for hydrogenation. J Am Chem Soc. 1930;52(11):4349-58.
73. Winans CF. Nickel as a Catalyst for the Hydrogenation of Aromatic Halogen Compounds. J Am Chem Soc. 1939;61(12):3564-5.
74. Soutelo-Maria A, Dubois J-L, Couturier J-L, Brebion M, Cravotto G. Regeneration of Raney®-Nickel Catalyst for the Synthesis of High-Value Amino-Ester Renewable Monomers. Catalysts. 2020;10(2).
75. Jiang H, Lu S, Zhang X, Dai W, Qiao J. Polymer-Supported Raney Nickel Catalysts for Sustainable Reduction Reactions. Molecules (Basel, Switzerland). 2016;21(7):833.
76. Basaveni S, Kuchkina NV, Shifrina ZB, Pal M, Rajadurai M. Ni nanoparticles on polyaromatic hyperbranched polymer support as a mild, tunable, and sustainable catalyst for catalytic transfer hydrogenation. J Nanopart Res. 2019;21(5):91.
77. Rachapudy H, Smith GG, Raju VR, Graessley WW. Properties of amorphous and crystallizable hydrocarbon polymers. III. Studies of the hydrogenation of polybutadiene. Journal of Polymer Science: Polymer Physics Edition. 1979;17(7):1211-22.
78. Tsai WH, Young JT, Boerio FJ, Hong PP. Characterization of model polyimide/silver interphases using surface-enhanced Raman scattering. Langmuir. 1991;7(4):745-54.
79. Zhang M, Kim HK, Chalkova E, Mark F, Lvov SN, Chung TCM. New Polyethylene Based Anion Exchange Membranes (PE–AEMs) with High Ionic Conductivity. Macromolecules. 2011;44(15):5937-46.

80. Vandiver MA, Caire BR, Pandey TP, Li Y, Seifert S, Kusoglu A, et al. Effect of hydration on the mechanical properties and ion conduction in a polyethylene-b-poly(vinylbenzyl trimethylammonium) anion exchange membrane. J Membr Sci. 2016;497:67-76.
81. Kim YS. Polymer Electrolytes with High Ionic Concentration for Fuel Cells and Electrolyzers. ACS Appl Polym Mater. 2021;3(3):1250-70.
82. Luo X, Kushner DI, Li J, Park EJ, Kim YS, Kusoglu A. Anion Exchange Ionomers: Impact of Chemistry on Thin-Film Properties. Adv Funct Mater. 2021;31(20):2008778.
83. Li D, Motz AR, Bae C, Fujimoto C, Yang G, Zhang F-Y, et al. Durability of anion exchange membrane water electrolyzers. Energy Environ Sci. 2021;14(6):3393-419.
84. Chu B, Hsiao BS. Small-Angle X-ray Scattering of Polymers. Chem Rev. 2001;101(6):1727-62.
85. Richards RW, Thomason JL. Small-angle neutron scattering study of block copolymer morphology. Macromolecules. 1983;16(6):982-92.
86. Audichon T, Mayousse E, Napporn TW, Morais C, Comminges C, Kokoh KB. Elaboration and characterization of ruthenium nano-oxides for the oxygen evolution reaction in a Proton Exchange Membrane Water Electrolyzer supplied by a solar profile. Electrochim Acta. 2014;132:284-91.
87. Min X, Shi Y, Lu Z, Shen L, Ogundipe TO, Gupta P, et al. High performance and cost-effective supported IrOx catalyst for proton exchange membrane water electrolysis. Electrochim Acta. 2021;385:138391.
88. Dong Y, Komarneni S. Strategies to Develop Earth-Abundant Heterogeneous Oxygen Evolution Reaction Catalysts for pH-Neutral or pH-Near-Neutral Electrolytes. Small Methods. 2021;5(1).

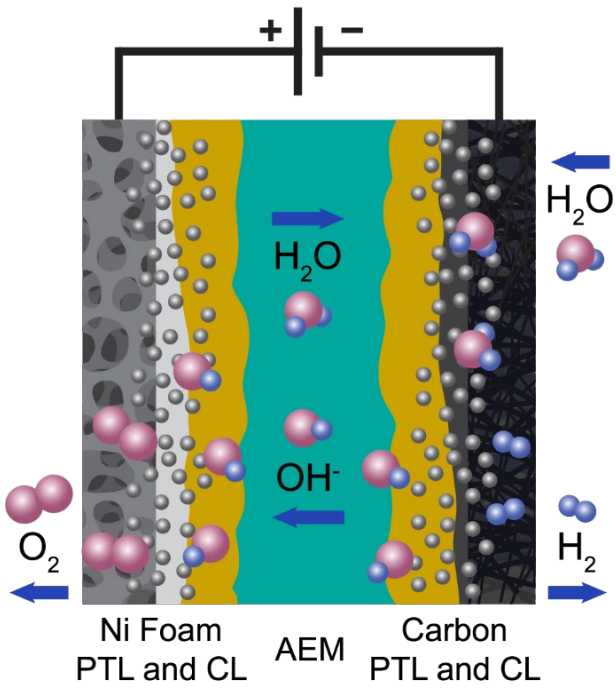

Figure 1. Diagram of an anion exchange membrane (AEM) water electrolysis cell, including detailed interfaces of the Ni foam and carbon paper porous transport layers (PTLs) and catalyst layers (CLs).

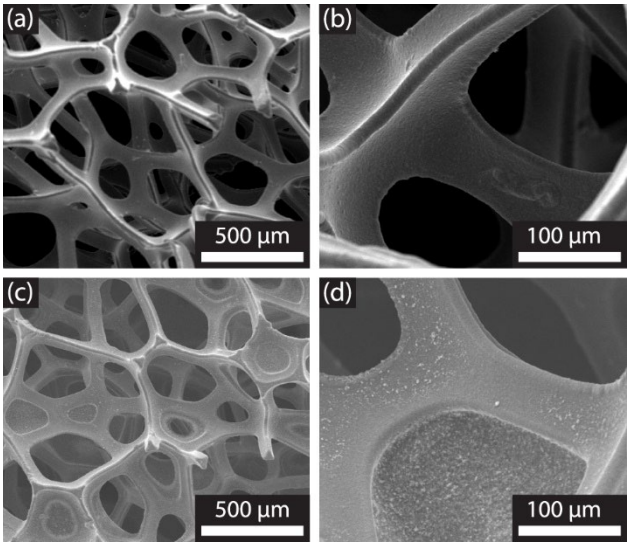

Figure 2. SEM images of pristine nickel foam (a,b) and representative as-deposited Ag-ionomer catalyst ink on Ni foam (c,d).

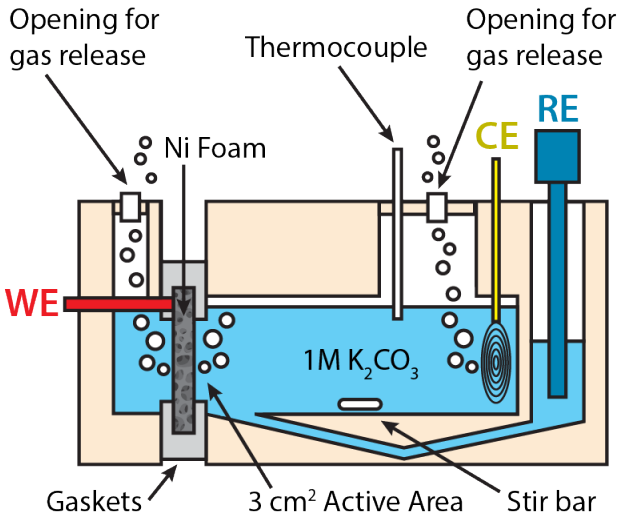

Figure 3. Cross-sectional diagram of the FlexCell® half-cell electrochemical measurement apparatus.

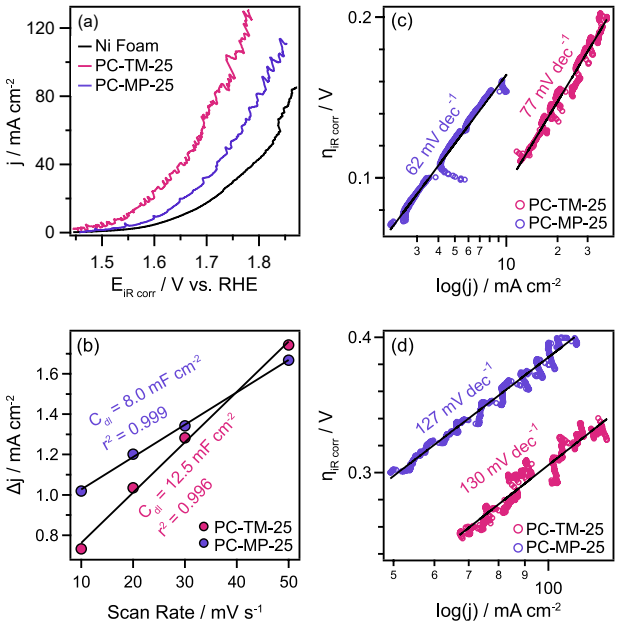

Figure 4. iR corrected LSVs (a), double layer capacitance (b), and Tafel Plots at low (c) and high (d) overpotential comparing PC-TM-25 and PC-MP-25.

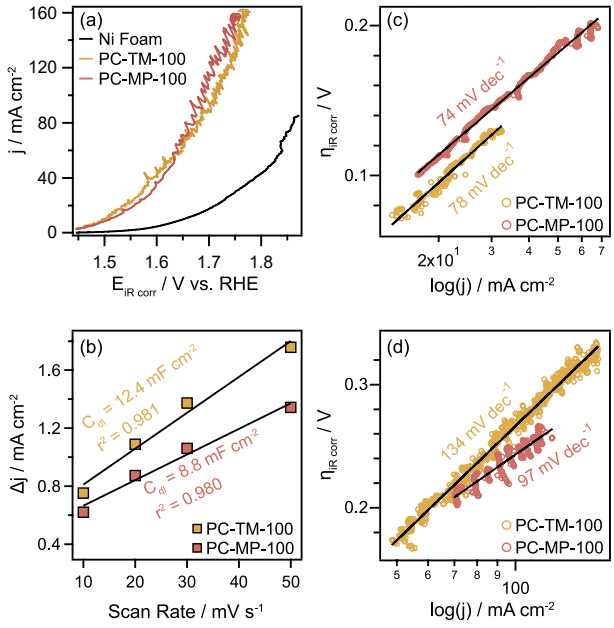

Figure 5. iR Corrected LSVs (a), double layer capacitance (b), and Tafel Plots at low (c) and high (d) overpotential comparing PC-TM-100 and PC-MP-100.

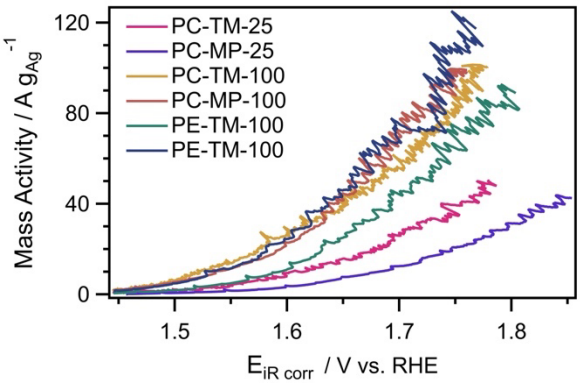

Figure 6. Mass activity (per gram Ag catalyst) comparing all samples investigated.

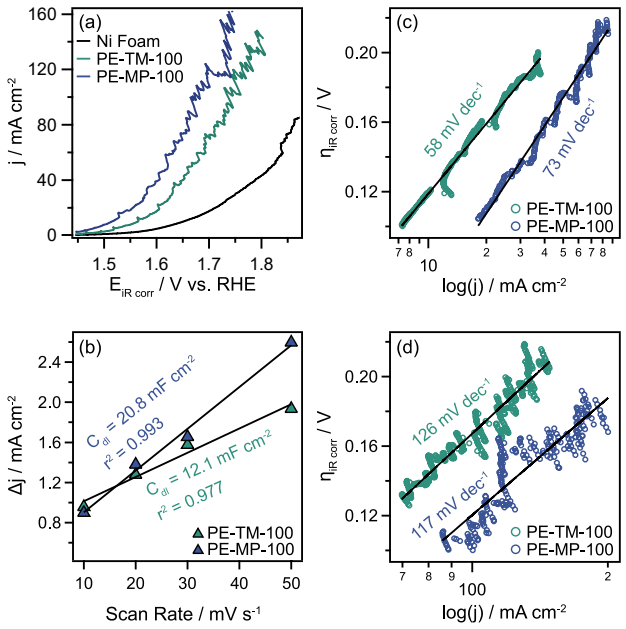

Figure 7. iR Corrected LSVs (a), double layer capacitance (b), Tafel Plots at low (c) and high (d) overpotential comparing PE-TM-100 and PE-MP-100.

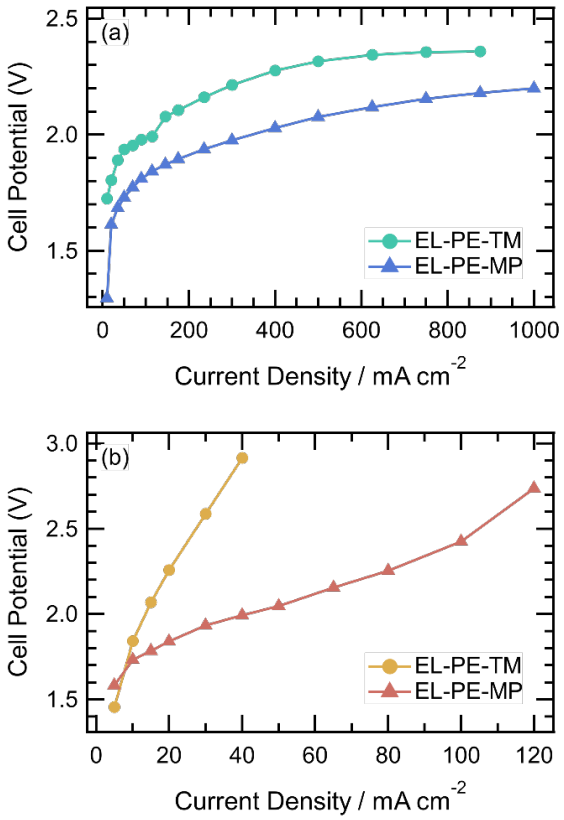

Figure 8. Polarization curves for AEM electrolyzers EL-PE-TM and EL-PE-MP in 1 M K_2CO_3 (a) or DI H_2O (b) at 50 °C with iR correction. 60% iR correction was used for polarization curves in 1 M K_2CO_3 and 100% iR correction was used for polarization curves in DI H_2O.

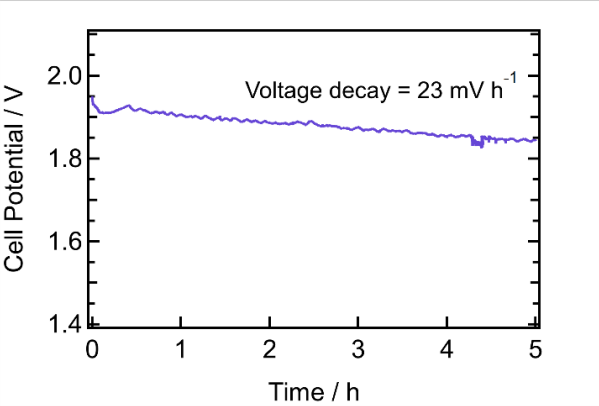

Figure 9. Voltage degradation of EL-PE-MP electrolyzer. The current density of the cell was held constant at 500 mA cm^{-2} for a duration of 5 h.